Am J Physiol Cell Physiol 319: C136–C147, 2020.
First published May 13, 2020; doi:10.1152/ajpcell.00405.2019.

METHODS IN CELL PHYSIOLOGY | *Making Cell Culture More Physiological*

Effect of luminal flow on doming of mpkCCD cells in a 3D perfusable kidney cortical collecting duct model

Joshua L. Rein,[1] Szilvia Heja,[2] Daniel Flores,[2] Rolando Carrisoza-Gaytán,[2] Neil Y. C. Lin,[3] Kimberly A. Homan,[3] Jennifer A. Lewis,[3] and Lisa M. Satlin[2]

[1]*Division of Nephrology, Department of Medicine, Icahn School of Medicine at Mount Sinai, New York, New York;* [2]*Division of Pediatric Nephrology and Hypertension, Department of Pediatrics, Icahn School of Medicine at Mount Sinai, New York, New York; and* [3]*School of Engineering and Applied Sciences, Wyss Institute for Biologically Inspired Engineering, Harvard University, Cambridge, Massachusetts*

Submitted 24 September 2019; accepted in final form 11 May 2020

Rein JL, Heja S, Flores D, Carrisoza-Gaytan R, Lin NYC, Homan KA, Lewis JA, Satlin LM. Effect of luminal flow on doming of mpkCCD cells in a 3D perfusable kidney cortical collecting duct model. *Am J Physiol Cell Physiol* 319: C136–C147, 2020. First published May 13, 2020; doi:10.1152/ajpcell.00405.2019.—The cortical collecting duct (CCD) of the mammalian kidney plays a major role in the maintenance of total body electrolyte, acid/base, and fluid homeostasis by tubular reabsorption and excretion. The mammalian CCD is heterogeneous, composed of Na^+-absorbing principal cells (PCs) and acid-base-transporting intercalated cells (ICs). Perturbations in luminal flow rate alter hydrodynamic forces to which these cells in the cylindrical tubules are exposed. However, most studies of tubular ion transport have been performed in cell monolayers grown on or epithelial sheets affixed to a flat support, since analysis of transepithelial transport in native tubules by in vitro microperfusion requires considerable expertise. Here, we report on the generation and characterization of an in vitro, perfusable three-dimensional kidney CCD model (3D CCD), in which immortalized mouse PC-like mpkCCD cells are seeded within a cylindrical channel embedded within an engineered extracellular matrix and subjected to luminal fluid flow. We find that a tight epithelial barrier composed of differentiated and polarized PCs forms within 1 wk. Immunofluorescence microscopy reveals the apical epithelial Na^+ channel ENaC and basolateral Na^+/K^+-ATPase. On cessation of luminal flow, benzamil-inhibitable cell doming is observed within these 3D CCDs consistent with the presence of ENaC-mediated Na^+ absorption. Our 3D CCD provides a geometrically and microphysiologically relevant platform for studying the development and physiology of renal tubule segments.

3D cortical collecting duct model; cell physiology; ENaC; fluid shear stress; principal cell

INTRODUCTION

The collecting duct (CD) of the mammalian kidney plays a major role in the maintenance of total body electrolyte, acid/base and fluid homeostasis, and control of blood pressure (9, 41, 63, 65, 72, 91). The CD is divided into three major segments: the cortical CD (CCD), the outer medullary CD (OMCD), and the inner medullary CD (IMCD) (43). Satlin and coworkers have long focused on the CCD (9, 11, 12, 76, 78, 79, 99), a heterogenous nephron segment within the aldosterone-sensitive distal nephron (ASDN) composed of two major cell populations, principal cells (PCs) and intercalated cells (ICs), each with distinct functions. PCs mediate transepithelial Na^+ and water reabsorption as well as basal K^+ secretion (65). These cells express the epithelial Na^+ channel ENaC and the secretory renal outer medullary K^+ channel ROMK and stretch/Ca^{2+}-activated large conductance BK channel on the apical plasma membrane. Transepithelial transport of Na^+ and K^+ requires robust basolateral Na^+-K^+-ATPase activity. Water reabsorption by PCs is triggered by vasopressin-stimulated insertion of the water channel aquaporin 2 (AQP2) into the apical plasma membrane. ICs function in acid-base transport, Na^+ and Cl^- reabsorption, and K^+ transport (direction determined by metabolic needs) (68, 72). Three subtypes of ICs have been identified: *1*) type A (H^+ secretion via apical H^+-ATPase), *2*) type B (HCO_3^- secretion and NaCl reabsorption via the apical Cl^-/HCO_3^- exchanger pendrin and the apical Na^+-dependent Cl^-/HCO_3^- exchanger NDCBE, respectively), and *3*) non-A, non-B (transitional cell with mixed function), all primarily energized by a H^+-ATPase. Cells in the CD have been proposed to interconvert between ICs and PCs (14, 57, 64). Notably, cultured CD cells can express PC specific, IC specific, or both types of markers (3, 22), consistent with evidence of plasticity between PC and IC phenotypes (14, 57, 64).

The gold standard for measuring renal transepithelial tubular transport and examining the molecular physiology of proteins mediating transport has been the technique of in vitro microperfusion of well-defined nephron segments isolated from kidneys of mouse, rat, and rabbit (7, 8, 25). However, only a few laboratories across the world are capable of carrying out these technically demanding experiments. By contrast, two-dimensional (2D) epithelial monolayers cultured under static condition or isolated split open tubules have long been used to study renal physiology and pathophysiology at the cellular level but fail to recapitulate the complex microphysiological environment that key segments of the nephron experience in vivo. It is now well accepted that mechanical forces affect structure, function, and differentiation of kidney tubular epithelial cells (9, 29, 76). As such, superfusate flow over 2D cell monolayers, associated with fluid shear stress (FSS) and drag/torque on cilia (51, 94), influences expression and activation of solute transport proteins and improves the physiologic rele-

---

Correspondence: J. L. Rein (joshua.rein@mssm.edu).

vance of the model compared with static culture (21, 23, 32, 33, 67). However, increases in luminal flow rate in the ASDN, as may be induced by extracellular volume expansion, diuretics, or a high K^+ diet in mammalian cylindrical tubules in vivo (10) and in vitro (100), lead to circumferential stretch (CS) (51) as well as FSS and drag/torque on specialized apical protrusions in PCs and ICs (94), hydrodynamic forces which differentially regulate intracellular signaling pathways involved in tubular transport (10, 23). Consequently, 2D culture cannot predict in vivo tissue functions that arise in 3D geometries.

Three-dimensional (3D) kidney models are useful microphysiological systems for studying tissue development, physiology, and disease states (29, 30, 49, 50, 69). Recently, 3D proximal tubule-on-chip models have been reported, which demonstrate that renal epithelial cells seeded in channels embedded within an engineered extracellular matrix (ECM) and exposed to continuous fluid flow exhibit improved phenotype, morphology, and function compared with those in flat monolayers cultured under static or flow conditions on plastic or ECM (30, 50). Building on this work, we have developed a perfusable 3D kidney CCD model (3D CCD) that consists of a straight channel embedded within an ECM that is seeded with mpkCCD cells, a well characterized cell line resembling PCs (4) (Fig. 1 and Supplemental Fig. S1; all Supplemental material is available at https://doi.org/10.5281/zenodo.3891813). Analysis of these 3D CCDs reveals a tight epithelial barrier with a differentiated and polarized phenotype. Specifically, our observations of immunodetectable apical ENaC and basolateral Na^+/K^+-ATPase and benzamil (BZ)-inhibitable cell doming in these 3D CCDs suggests that they support ENaC-mediated transepithelial Na^+ transport and can be used to explore the molecular mechanisms responsible for regulation of transport in this segment.

METHODS

Cell culture. mpkCCD cells were grown in modified Dulbecco's modified Eagle's medium (DMEM):Ham's F-12, 1:1 vol/vol (120 mM NaCl, 29 mM $NaHCO_3$, 4.2 mM KCl, 1.1 mM $CaCl_2$, 0.7 mM $MgSO_4$, 0.5 mM NaH_2PO_4, and 0.5 mM Na_2HPO_4), 20 mM HEPES, pH 7.4, 20 mM D-glucose, and 2 mM glutamine, supplemented with 60 nM sodium selenite, 5 μg/mL transferrin, 50 nM dexamethasone, 1 nM triiodothyronine, 10 ng/mL epidermal growth factor, 5 μg/mL insulin, 2% fetal calf serum, and 1% penicillin/streptomycin) (4) in T-25 flasks up to passage 14 to limit genetic drift. Cells were passaged ~2–3 days after confluence when cells began to form domes. mpkCCD cells were selected since they show aldosterone- and vasopressin-sensitive upregulation of Na^+/K^+-ATPase, ENaC, and AQP2 expression and activity (4, 71) as well as secrete prostaglandin E_2, a paracrine/autocrine signaling factor in the CCD whose release is enhanced in response to increases in FSS (23). The mpkCCD transcriptome (71), proteome (74, 80), and phosphoproteome (70) have also been extensively studied.

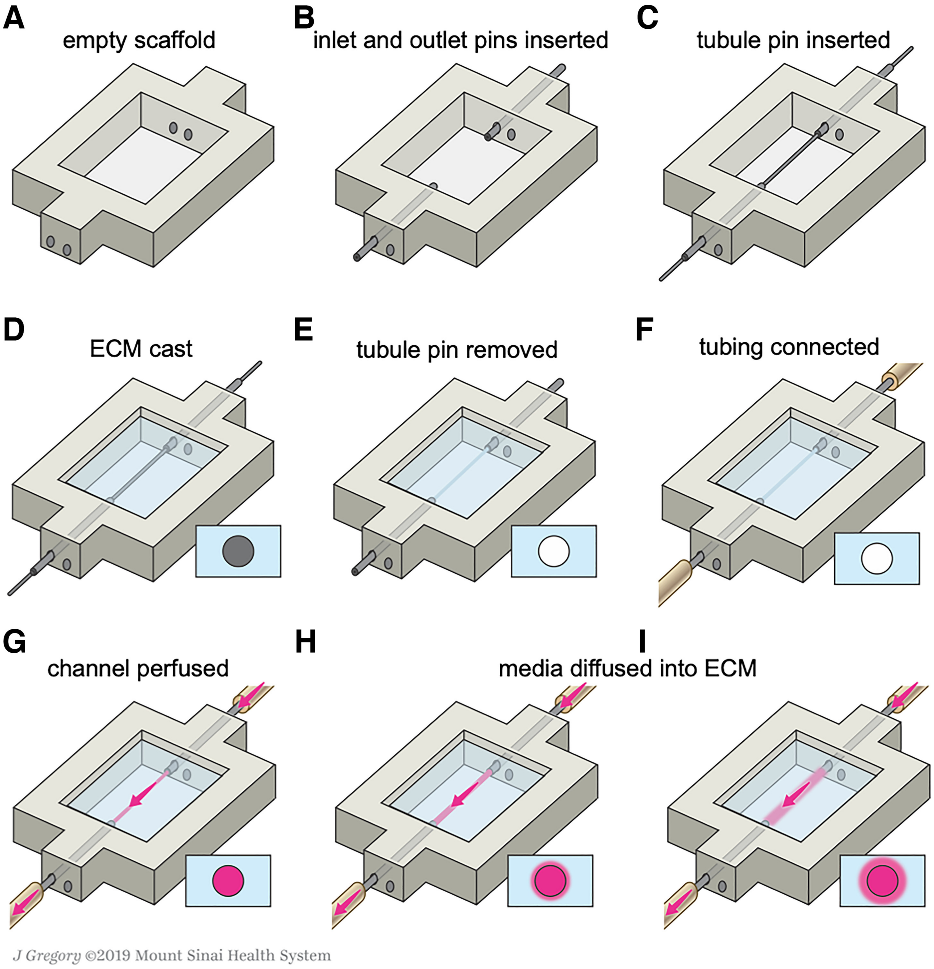

Fig. 1. Schematic illustrations of the kidney chip taken after completion of each fabrication step (*A–I*) used to create the 3D CCD model. ECM, extracellular matrix. [Printed with permission from ©Mount Sinai Health System.]

3D model fabrication. 3D CCD models were housed within a printed silicone gasket-on-chip (Fig. 1*A* and Supplemental Fig. S1*A*). This gasket was produced by loading the silicone ink into a 30-ml syringe, centrifuging to remove air bubbles, and printing through a tapered 410-μm nozzle (EFD Nordson, East Providence, RI) at a print speed of 30 mm/s. The gasket was designed in SolidWorks (Dassault Systèmes, Vélizy-Villacoublay, France) and printed onto 50 mm × 75 mm glass slides (Corning Inc., Corning, NY) using a custom-designed 3D bioprinter equipped with a printhead mounted onto a three-axis, motion-controlled gantry (Aerotech, Inc., Pittsburgh, PA). The silicone gasket was then cured at 80°C in a convection oven overnight and stored at room temperature. Stainless-steel tubes (20.5G, Hamilton Company, Reno, NV) were then inserted through the PDMS scaffold on opposite ends to serve as inlet and outlet conduits (Fig. 1*B* and Supplemental Fig. S1*B*). A 510 μm stainless-steel pin (25G), i.e., a "tubule pin", was inserted through these conduits and spanned the length of the silicone border (Fig. 1*C* and Supplemental Fig. S1*C*). The assembled construct was autoclaved before use and assembled in a sterile field.

The reservoir housed within the chip was filled with a hydrogel extracellular matrix (ECM) composed of a gelatin and fibrin network crosslinked with transglutaminase (TG) and thrombin. Before this procedure, a gelatin solution (15 wt/vol%) (Type A, 300 bloom from porcine skin, Sigma-Aldrich, St. Louis, MO) was produced by adding gelatin powder to 1× phosphate-buffered saline without Ca^{2+} and Mg^{2+} (PBS) at 70°C. The gelatin was fully dissolved by continuous stirring at 70°C for 12 h, and its pH was adjusted to 7.5 using 1 M NaOH. The solution was sterile filtered and stored at 4°C in aliquots for future use. Next, a fibrinogen solution (40 mg/mL) was produced by dissolving lyophilized fibrinogen (bovine plasma, Millipore, Burlington, MA) in sterile PBS at 37°C. The solution was held at 37°C for 1–2 h and stored at −20°C. TG solution (60 mg/mL) was prepared by dissolving lyophilized powder (Moo Gloo TI Formula, Modernist Pantry, Eliot, ME) in PBS and mixing for 10 s. The solution was then held at 37°C for 20 min and sterile filtered before using. A $CaCl_2$ stock solution (250 mM) was prepared by dissolving $CaCl_2$ in sterile water. The thrombin stock solution was prepared by reconstituting lyophilized thrombin (MP Biomedicals, Solon, OH) at 500 U/mL with sterile PBS and stored at −20°C. The final ECM solution was produced by combining these constituents in 7.5 pH adjusted 1× PBS to yield concentrations of 25 mg/mL fibrinogen, 1 wt/vol% gelatin, 2.5 mM $CaCl_2$, and 0.2 wt/vol% TG. This solution was then equilibrated at 37 °C for 15–20 min and pH adjusted to ~7.5 with 1 M NaOH before use to improve optical clarity of the ECM (42). Before ECM casting, sterile glycerol was applied to the tubule pin to minimize adhesion. The ECM solution was then rapidly mixed with thrombin at a ratio of 200:1, resulting in a final thrombin concentration of 3 U/mL and immediately placed within the chip reservoir such that the tubule pin was fully immersed within the ECM (Fig. 1*D* and Supplemental Fig. S1*D*). The chip was then covered by a plastic dish to prevent evaporation and contamination and held at 37 °C for 1 h to allow for fibrin polymerization and crosslinking of the fibrin/gelatin network. Afterwards, the tubule pin was removed through the outlet conduit, leaving a hollow channel embedded within the ECM-on-chip (Fig. 1*E* and Supplemental Fig. S1*E*). To complete the chip assembly, these constructs were encased between a machined stainless-steel base and a thick acrylic lid that were clamped together by four screws that formed a tight seal around the printed and infilled features.

The fabricated 3D chips were then connected to external cell culture media reservoirs to enable media flow and cell seeding within the channel. Unless prepackaged sterilely, each component described below was autoclaved before use. A 10-ml syringe barrel and adapter assembly (EFD Nordson, East Providence, RI) with a 0.20-μm syringe filter (Corning Inc., Corning, NY) served as a media reservoir. Microbore silicone tubing (0.50-mm inner diameter) (Cole-Parmer, Vernon Hills, IL) connected the reservoir to the pump inlet, the pump outlet to the chip inlet, and the chip outlet back to the reservoir (Fig. 1*F* and Supplemental Fig. S1*F*). The circuit was primed and perfused with mpkCCD media containing 1% aprotinin (bovine lung, crystalline, Millipore, Burlington, MA), to prevent cellular degradation of the ECM, with a peristaltic pump (P-70, Harvard Apparatus, Holliston, MA) using three-stop PharMed BPT tubing (0.25 mm ID) (Cole-Parmer, Vernon Hills, IL). Polypropylene pinch clamps were added to the silicone tubing to prevent uncontrolled flow when the circuit was disconnected from the pump such as during cell culture media changes. The 3D CCD model was then placed in the incubator and perfused with media for 24 h before cell seeding (Fig. 1, *G–I*, and Supplemental Fig. S1*G–I*) to fully saturate the ECM with media. The media reservoir was equilibrated with atmospheric incubator conditions by means of a sterile filter on top of the reservoir. The printing and pin-pullout technique to create a perfusable channel embedded within the ECM as well as its subsequent perfusion of cell culture media is highlighted in Supplemental Video S1.

To seed the channel with cells, mpkCCD cells were trypsinized from flasks and concentrated in cell culture media to a density of ~2 × 10^6 cells/mL. The cell suspension was then injected into the empty channel through the outlet (Fig. 2, *A* and *B*) and the construct was kept in the incubator at 37°C and 5% CO_2 for 16 h without flow. The next day, nonadherent cells were flushed out (Fig. 2*C*), and perfusion of fresh media was begun at a continuous, unidirectional peristaltic flow rate of 8.33 μL/min, equating to a physiologic FSS for the CCD of 0.1 dyn/cm² (51) as calculated by the Hagen-Poiseuille equation: $Q = \pi P r^4 / 8\eta l$, where Q is the volumetric flow rate (L/s), P is pressure (Pa), r is the cylinder radius (m), η is the viscosity (cP), and l is the cylinder length (m). Reservoir medium was changed every 2 days. Experiments were performed 7 days after cell seeding.

Immunostaining. Cellular localization of PC-specific proteins in cell monolayers grown on glass coverslips and within the 3D CCD were examined by immunofluorescence and confocal microscopy after 7 days of cell growth. Samples were fixed with 4% paraformaldehyde in PBS and stored in 0.05% sodium azide in PBS at 4°C until processing. After storage, samples were washed in PBS for 1 h and sectioned freehand with a razorblade into 1- to 2-mm thick slices. Cells were permeabilized with 0.3% Triton X-100 for 10 min then blocked with blocking solution (1% BSA, 10% FBS, and 0.1% Triton X-100 in PBS) for 1 h. Primary antibodies (1° ab) (Table 1) were diluted in ab solution (blocking solution diluted 1:10), incubated at 4°C overnight, and then washed for three times for 5 min in PBS. An appropriate Alexa-Fluor 488-conjugated 2° ab (Thermo-Fisher, Waltham, MA) (goat anti-rabbit IgG for ENaCα, ENaCβ, and AQP2; goat anti-chicken IgG for BKα) was diluted in ab solution (1:250), applied for 2 h, and then washed three times for 5 min in PBS. Rhodamine phalloidin in PBS (1:500) was applied for 2 h and then washed three times for 5 min in PBS. 4′,6-Diamidino-2-phenylindole (DAPI) in PBS (1:10,000) was applied for 30 min then washed, and samples were stored in PBS before imaging. Confocal microscopy was performed with a Leica SP5 DM with HCX APO L U-V-I ×20/0.5 and ×40/0.8 water dipping objectives. Stacks of confocal sections were obtained and processed using Leica Application Suite (LAS AF) software (Leica Microsystems, Wetzlar, Germany). Before 3D rendering of the en bloc 3D CCD section, confocal images were processed by applying an adaptive blind deconvolution algorithm using a theoretical point spread function in AutoQuant X3 (v.X3.1.3. Media Cybernetics, Rockville, MD), and 3D rendering was done in Imaris (v.9.2.1. Bitplane, Concord, MA).

Electron microscopy. Transmission electron microscopy was performed after 7 days of cell growth to visualize cellular details of the 3D CCD at high resolution. Samples were fixed in 2% glutaraldehyde for 16 h. Following a routine protocol, the sample was embedded in an Epon-Araldite resin and cut into ultrathin (~60–80 nm) sections, in which osmium tetroxide was used for enhancing the contrast. Samples were imaged with a Tecnai G2 Spirit BioTWIN Transmission Electron Microscope.

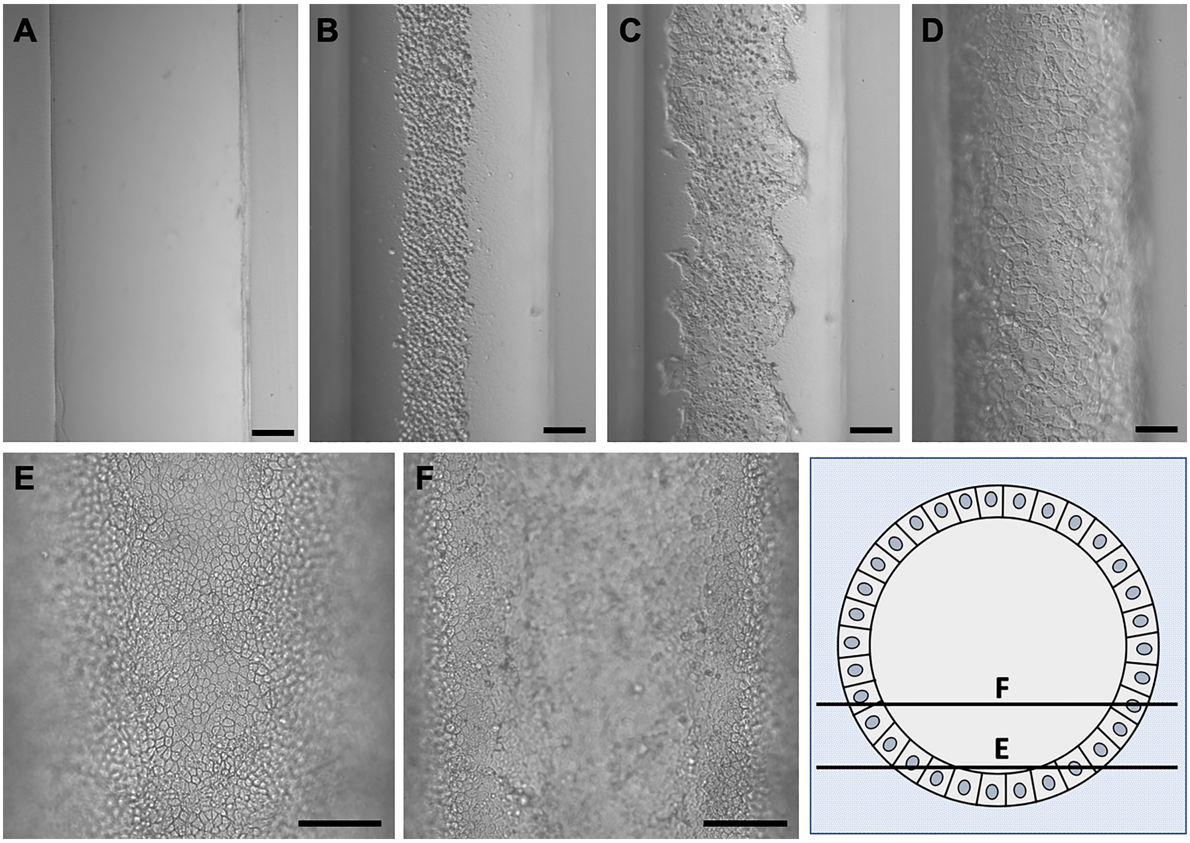

Fig. 2. Epithelialization of the 3D CCD. *A*: an empty channel. *B*: mpkCCD cells in the channel immediately after cell seeding. *C*: cell growth 1 day after cell seeding. *D*: epithelialized channel after 7 days (differential interference contrast microscopy at ×10. Scale bar = 100 μm). *E* and *F*: cell growth in the 3D CCD after 7 days imaged at different focal planes to demonstrate the three dimensionality of the cell growth around the circumference of the channel (phase contrast microscopy at ×20. Scale bar = 100 μm).

Histological staining. 3D CCDs were fixed with 4% paraformaldehyde in PBS and stored in 0.05% sodium azide in PBS at 4°C before processing. After storage, 3D CCDs were washed in PBS for 1 h and sectioned freehand with a razorblade into 1- to 2-mm thick slices. Samples were embedded in paraffin wax, sectioned, and exposed to Masson's trichrome stain. Bright-field microscopy was performed with a Zeiss Axio Imager.Z2M widefield microscope with a plan-apochromat/1.40 oil objective.

Diffusional permeability measurements. Epithelial integrity of the 3D CCD was evaluated by perfusion at 0.1 dyn/cm^2 of 25 μM 3- to 5-kDa fluorescein isothiocyanate (FITC)-dextran (Sigma-Aldrich, St. Louis, MO) in cell culture media in three channels with or without cells. Images were taken before perfusion then every 10 min for 1 h during perfusion using widefield microscopy with a stage top incubator (Tokai Hit model WSKM, Shizuoka-ken, Japan) set to 37°C and 5% CO$_2$ on a Leica DMi8 inverted widefield microscope with a Leica DFC9000 GT sCMOS camera with a HC semi-apochromat Fluotar ×1.25/0.04 dry objective or HC PL Fluotar ×10/0.32 dry objective. Diffusional permeability of the 3- to 5-kDa FITC-dextran was calculated by quantifying changes in fluorescence intensity over time using the following equation: $P_{\mathrm{d}} = \frac{1}{I_1 - I_{\mathrm{b}}}\left(\frac{I_2 - I_1}{t}\right)\frac{d}{4}$, as previously described (66), where P_{d} is the diffusional permeability coefficient, I_1 is the average intensity at an initial time point, I_2 is an average intensity at a later time point, I_{b} is background intensity (image taken before perfusion of FITC-dextran), and d is the channel diameter. Image acquisition and analysis were performed using Leica Application Suite X.

Table 1. *Primary antibodies used for immunofluorescence*

1° Antibody	Source
Anti-acetylated α-tubulin (Lys40) rabbit monoclonal IgG (1:800)	Cell Signaling (no. 5335)
Anti-AQP2 rabbit polyclonal IgG (1:50)	Alomone Laboratories (AQP-002)
Anti-BKα chicken polyclonal IgG (1:100)	Satlin Laboratory (101) (Aves Laboratories)
Anti-ENaCα rabbit polyclonal IgG (1:50)	StressMarq Biosciences (SPC-403)
Anti-ENaCβ rabbit polyclonal IgG (1:50)	StressMarq Biosciences (SPC-404)
Anti-Na$^+$/K$^+$-ATPase rabbit monoclonal IgG (1:50)	Abcam (ab76020)

AQP2, aquaporin 2; ENaC, epithelial Na$^+$ channel.

Doming measurements. To study cell doming in the 3D CCD model, a 1-mm channel segment at the chip inlet was imaged during both perfusion under a FSS of 0.1 dyn/cm^2 and under static conditions for 1 h after stopping flow in the absence (control) or presence of luminal 1 μM BZ hydrochloride (Sigma-Aldrich, St. Louis, MO), an inhibitor of ENaC (39), for 16 h. These experiments were repeated in chips fabricated with an additional channel (300 μm in diameter) that was located adjacent to the 3D CCD (~2.5 mm center-to-center separation distance), which served as a drainage channel open to atmospheric pressure. Images were obtained with live cell phase contrast and differential interference contrast microscopy with a HC PL Fluotar ×10/0.32 dry objective, HC PL Fluotar L ×20/0.40 dry objective, or HC PL Fluotar L ×40/0.60 dry objective. Image acquisition and analysis were performed using Leica Application Suite X. Dome length and width were measured in the x- and y-dimensions and the longer of the two was used to calculate radius. Dome height in the z-dimension was determined to be the vertical distance from the plane of focus in the cell monolayer adjacent to the dome to the plane of focus containing the cells at the dome peak. Dome volume was estimated using the volume formula for a segment of a sphere: $V = \frac{1}{6}\pi h(3a^2 + h^2)$, where h is height of the segment (μm) and a is radius of the segment base (μm).

Statistical analysis. Data are presented as means ± SE from individual experiments and as individual data points, as shown. Significance of differences was tested by unpaired Student's t test (SigmaPlot 12.5, Systat Software, San Jose, CA) and statistical significance was defined as P values ≤ 0.05.

RESULTS

Cell seeding and longitudinal culture of 3D CCDs. After introduction of mpkCCD cells into the lumen of the channel embedded in ECM, cells grew to confluency, beginning at the base of the channel, to circumscribe the entire open lumen over a period of 3–4 days (Fig. 2, *C* and *D*). The inner diameter of these 3D CCDs ranged from 450 to 600 μm, as determined by the tubule pin size and cell height. We note that their diameter is roughly an order of magnitude higher than that observed for adult human (35–75 μm) (26, 45, 104), rabbit (35–40 μm) (77, 95, 96), and mouse (25–30 μm) CCDs (56). A time sequence of the cell growth in the channel is provided (Fig. 2). By 5–7 days, epithelialized channels took on a cobblestone appearance (Fig. 2, *D–F*), similar to that of the native CD (27, 28). Cell height averaged 11.6 ± 0.2 μm in three channels at 7 days (n = 16 or 17 cells/channel), consistent with in vivo human CD cells (60) and significantly exceeded the cell height of 7.0 ± 0.2 μm of mpkCCD cells grown in 2D on glass coverslips at 7 days in the absence of flow (n = 12 cells/coverslip) ($P < 0.001$). Transmission electron microscopy (TEM) of mpkCCD cells in the 3D CCD at 7 days revealed apical microvilli, adherent junctions (Fig. 3*A*), and basal infoldings (Fig. 3*B*), characteristics of native PCs (77).

Localization of transport and structural proteins in the 3D CCD. After formation of a confluent epithelium within the model (>7 days) under the presence of continuous luminal flow, cell morphology of the 3D CCD was characterized using a combination of light, widefield fluorescence, and confocal microscopy. mpkCCD cells in mature 3D CCDs adopted a cuboidal morphology, as described for PCs of the CCD (58, 95). Cells lining the 3D CCD at 7 days appeared homogenous,

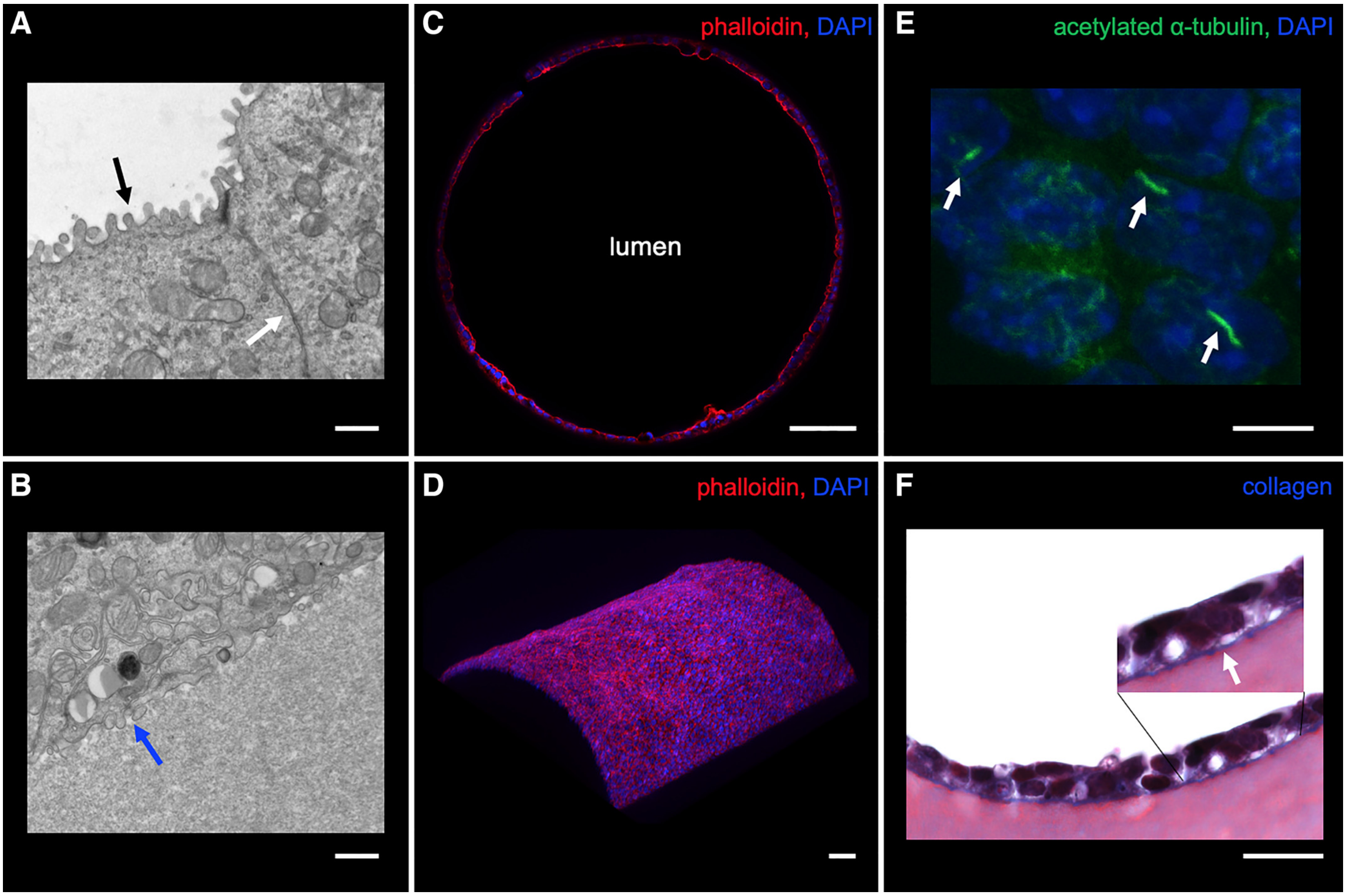

Fig. 3. Localization of structural proteins in the 3D CCD. *A* and *B*: transmission electron microscopy of mpkCCD cells in the 3D CCD demonstrating apical microvilli (black arrow), adherent junction (white arrow), and basal infoldings (blue arrow). Scale bar = 800 nm. *C*: strong apical F-actin localization in mpkCCD cells grown in the 3D CCD. Scale bar = 100 μm. *D*: 3D reconstruction revealing a curved epithelial monolayer as identified by F-actin staining. Scale bar = 100 μm. *E*: cells grown in the 3D CCD had immunodetectable cilia. Scale bar = 10 μm. *F*: cells deposit collagen along the basal surface onto the extracellular matrix (ECM) as identified by linear blue staining with Masson's trichrome and visualized by light microscopy. Scale bar = 20 μm.

unlike native CCDs that contain both PCs and ICs. Epithelial cell growth in a defined cylindrical compartment has been reported to enhance cellular organization, polarization, and actin alignment (52, 103). The apical actin cytoskeleton is important for cell polarization and regulates the activity of several transport proteins including AQP2 (32, 36, 81, 98), ENaC (2, 31, 53), and BK channels (87, 92). Immunofluorescence microscopy performed on fixed 3D CCD sections revealed predominantly apical F-actin localization identified by rhodamine phalloidin staining (Fig. 3*C*). Additionally, 3D reconstruction of F-actin staining revealed a curved epithelial monolayer (Fig. 3*D*). Note that many mpkCCD cells had detectable apical cilia (Fig. 3*E*) and expressed apical AQP2, the BKα subunit, α- and β-subunits of ENaC and basolateral Na$^+$/K$^+$-ATPase, consistent with the polarized phenotype of mammalian PCs (Fig. 4). Secondary ab controls on 3D CCD sections were negative for fluorescence (Supplemental Fig. S2). The native tubular basement membrane consists of collagen IV, laminin, and proteoglycans, which provide the principal structural support of renal tubules (54). Among intact tubules studied in vitro, the basement membrane is the main anatomic structure that limits their distensibility (97). Because collagen was not a component of the ECM used in these 3D CCDs, we were able to identify de novo collagen formation using Masson's trichrome stain, which revealed collagen deposition along the basal cell surface around the entire circumference of the epithelialized channel identified by blue staining, consistent with in vitro deposition of basement membrane by these cells (Fig. 3*F*).

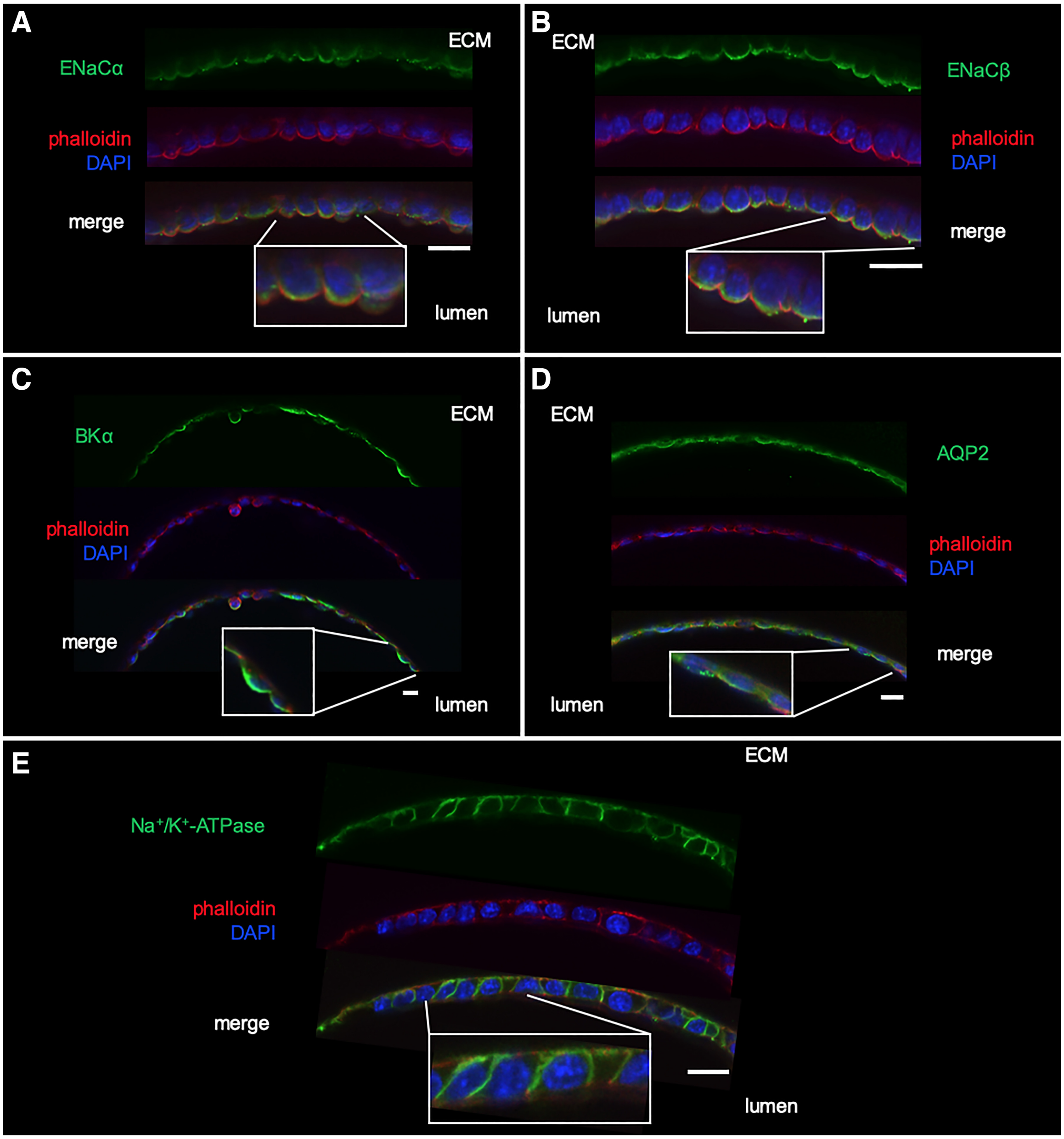

Fig. 4. Immunolocalization of relevant transport proteins in the 3D CCD. The 3D CCD expressed apical epithelial Na$^+$ channel (ENaCα) (*A*), ENaCβ (*B*), large conductance BKα (*C*), aquaporin 2 (AQP2) (*D*), and basolateral Na$^+$/K$^+$-ATPase (*E*), consistent with native mammalian principal cells. ECM, extracellular matrix.

Cell monolayer integrity. To confirm that the epithelized channels generated a tight monolayer, as is expected of the native mammalian CCD, we compared the diffusional permeability across empty and epithelialized channels. Empty channels and epithelialized channels after 7 days were perfused at 0.1 dyn/cm^2 with 3- to 5-kDa FITC dextran over 1 h. In empty channels, the fluorescent dye rapidly diffused into the surrounding ECM. In sharp contrast, the fluorescent dye was largely restricted to the lumen of the epithelialized channels over this same time period (n = 3) (Fig. 5*A*). The measured diffusional permeability of 3- to 5-kDa FITC dextran was significantly higher in the empty channel (n = 3) compared with the epithelialized channel (n = 3), i.e., P_d = 52.2 ± 13.1 μm/min without cells versus 1.9 ± 0.9 μm/min with cells (P = 0.01) (Fig. 5, *B* and *C*).

Doming. Cell doming is a unique feature of cultured epithelial cells that likely arises due to vectorial transport of Na$^+$, H$^+$, and water (44, 46, 47, 61, 83) and the subsequent accumulation of water underneath the cell monolayer (86). mpkCCD cells grown in 2D monolayers on glass coverslips form domes. However, cells grown under the same conditions on ECM, which is highly permeable to water, do not exhibit doming (Fig. 6*A*). To examine doming under 3D culture conditions on-chip, we first exposed the 3D CCDs to luminal 1 μM BZ during flow and static conditions. No doming was observed in any 3D CCD subjected to continuous fluid flow. However, doming was observed within 30 min of cessation of flow in all control 3D CCDs and in most of the BZ-treated 3D CCDs held at 37°C in 5% CO$_2$ (Fig. 6*B*). The mean number of domes/mm 3D CCD was lower in BZ-treated 3D CCDs (1.29 ± 0.42 domes/mm 3D CCD; n = 7) compared with controls (3.25 ± 0.48 domes/mm 3D CCD; n = 4; $P < 0.01$). Among the 3D CCDs that developed domes, the mean calculated dome volume was 4.57 ± 1.73 nl in controls (n = 4) compared with 0.55 ± 0.29 nl in BZ-treated 3D CCDs; n = 5; P = 0.01). As a primary function of PCs is to absorb Na$^+$ via ENaC, we speculate that doming arises due to ENaC-mediated Na$^+$ reabsorption and subsequent water absorption in a closed system.

We next explored the influence on dome formation of adding to our chip a drainage channel, anticipated to decrease hydrostatic pressure buildup within the ECM-on-chip, under the same flow and static conditions (Fig. 6*C*). Doming was observed after of cessation of flow in all control 3D CCDs and most of the epithelialized channels adjacent to a drainage channel (Fig. 6*D*). The mean number of domes/mm 3D CCD did not differ between controls and drainage 3D CCDs after cessation of flow (3.25 ± 0.48 versus 2.5 ± 0.96 domes/mm 3D CCD; P = 0.51) (Fig. 6*E*). However, despite similar dome number and domes/mm 3D CCD, mean dome volume was lower in the drainage 3D CCDs that demonstrated dome formation (n = 3) compared with controls after cessation of

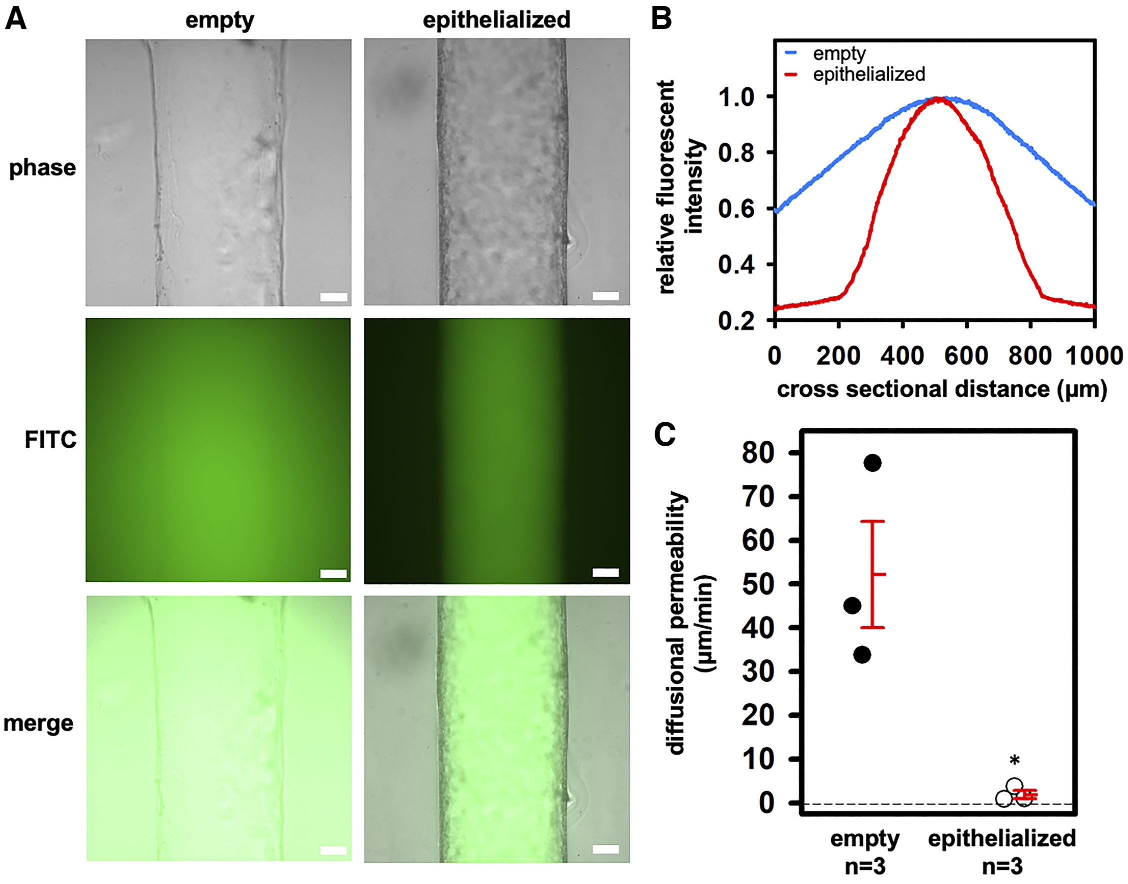

Fig. 5. Epithelial integrity assessed with 3- to 5-kDa FITC-dextran over 1 h. *A*: representative phase-contrast and widefield fluorescent images. Scale bar = 100 μm. *B*: histogram of mean fluorescence across the channel cross section showing tight barrier function to perfused 3- to 5-kDa FITC-dextran over 1 h. *C*: the diffusional permeability of the FITC-dextran was lower in epithelialized versus empty channels. Individual data points as well as means ± SE are shown. *P = 0.01 versus "empty."

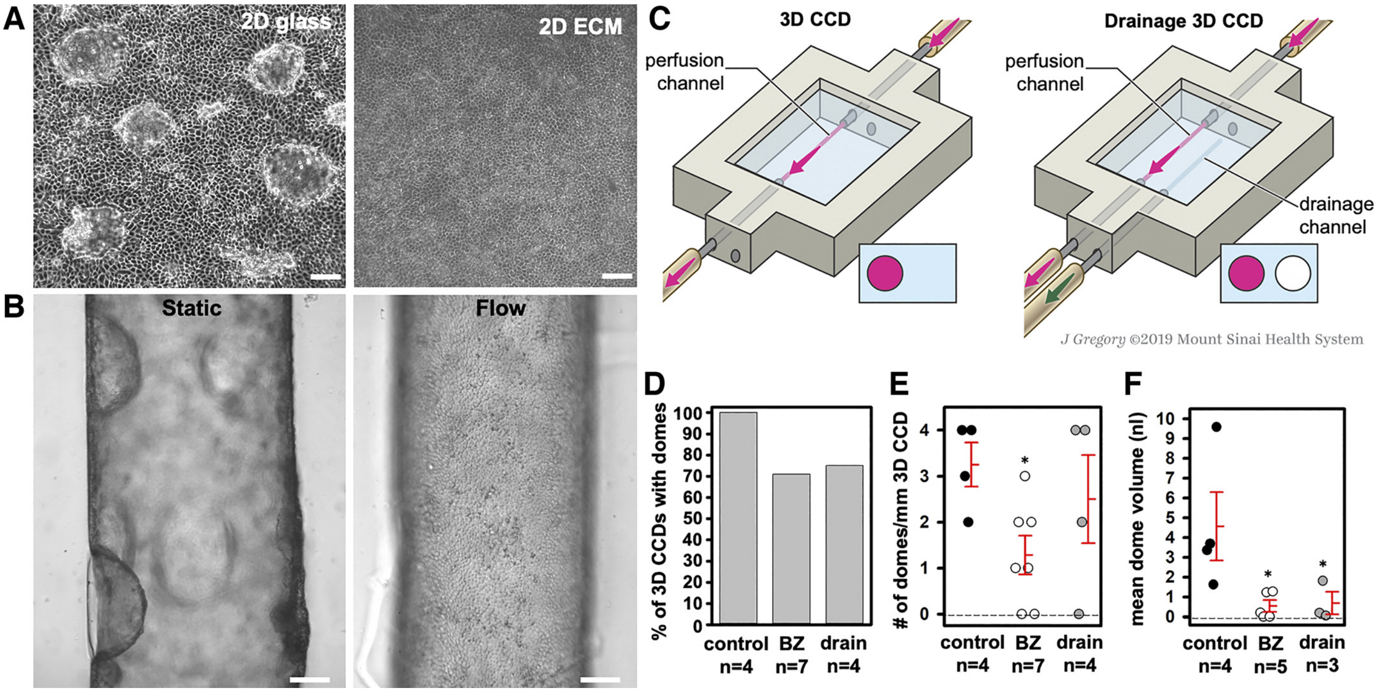

Fig. 6. Analysis of possible mechanisms underlying cell doming. *A*: mpkCCD cells grown on glass as 2-dimensional (2D) monolayers under static conditions formed domes spontaneously upon reaching cell confluence while cells grown on 2D ECM under static conditions did not (phase-contrast microscopy at ×10). Scale bar = 100 μm. *B*: in the 3D CCD, dome formation occurred in the absence of flow but did not occur with exposure to flow. Scale bar = 100 μm. *C*: schematic comparing the control to the drainage 3D CCD. *D*: the percentage of 3D CCDs with domes was not different among groups 1 h after stopping flow. *E*: the number of domes/mm 3D CCD was lower with 1 μM benzamil (BZ) compared with the control and drainage 3D CCDs. $^*P < 0.01$ vs. control. *F*: the mean dome volume was lower with 1 μM BZ or a drain vs. control 3D CCDs. $^*P < 0.01$ vs. control. Individual data points as well as means ± SE are shown in *E* and *F*. [Printed with permission from ©Mount Sinai Health System.]

flow (0.69 ± 0.56 nl vs. 4.57 ± 1.73 nl; $n = 4$; $P = 0.01$) (Fig. 6*F*). The latter results were similar to those observed in BZ-treated 3D CCDs.

DISCUSSION

We have developed an innovative microphysiological system to generate CCDs in a 3D geometry in which cells are placed within a cylindrical lumen and subjected to continuous luminal fluid flow. The pin-pullout technique (1, 16, 89) provides a simple way to create a straight channel embedded within a hydrogel matrix. Upon seeding with the appropriate cells, we generated a 3D CCD model that simulates the renal tubular microenvironment and allows for the study of the geometric and hydrodynamic effects on cell function (30, 50). Our 3D CCDs exhibited a tight epithelial barrier with a differentiated and polarized phenotype. Specifically, we identified immunodetectable cilia and appropriate polarized expression of apical channels (ENaC, BK, and AQP2) and basolateral Na^+/K^+-ATPase, characteristics of the native mammalian PC. Cells exhibited predominant apical F-actin, consistent with previous studies in tubular epithelial cells exposed to FSS (20, 32). Furthermore, the capacity of the 3D CCDs for ENaC-mediated Na^+ absorption and water transport are supported by our observation of BZ-inhibitable doming in epithelialized channels exposed to static and closed system conditions.

Cell doming is a characteristic unique to epithelial cell monolayers that occurs spontaneously in 2D culture (46). This phenomenon has been proposed to reflect cellular differentiation, cellular polarization, and vectorial transport of Na^+, H^+, and water (44, 46, 47, 61, 83). Doming occurs from the accumulation of water underneath the epithelial cells (86). Some cells respond to the increased tension by small-scale elastic deformations while other cells undergo large-scale superelastic deformations mediated by dilution of the cellular actin pool (44). Increased pressure within the dome eventually ruptures adhesive junctions between cells leading to water exit. Concomitantly, the dome collapses and cells return to their original shape (44). Mechanisms and characteristics of doming have been most extensively studied with Madin-Darby canine kidney (MDCK) cells, an immortalized epithelial cell line reflective of the distal nephron. Dome formation may be triggered by an increase in intracellular pH (19) upon reaching cell confluency by stat3-mediated induction of the Na^+/H^+ exchanger NHE3 (83, 84). Domed cells were shown to have high intracellular cAMP levels (19, 47) and generate a prostaglandin dependent decrease of Cl^- in dome fluid (48). Additionally, doming has been reported to be dependent on extracellular Na^+ (85), stimulated by aldosterone (38, 61) and inhibited with coadministration of spironolactone (38). Lastly, aldosterone generates alkaline dome fluid through increased activity of apical Na^+/H^+ exchange and Cl^-/HCO_3^- exchange (62).

The absence of cell doming under flow in our 3D CCD model is consistent with a 2D MDCK cell model that showed flow inhibition of dome formation was dependent on cilia and Ca^{2+} influx (13). While we did not observe doming among mpkCCD cells grown on our 2D ECM, the observation of doming in the 3D CCD when flow was stopped prompted us to explore possible mechanisms. Prior experiments with endothelial vascularized microphysiological systems showed improved cell adhesion using fibrin-based ECMs as well as lower cell delamination when empty drainage channel(s), akin to lymphatic drainage in vivo, are incorporated into organ-on-chip models (102). Accordingly, we introduced a drainage channel within our model and observed significantly smaller dome formation in the adjacent epithelialized channel, consistent with stabilized epithelial adhesion and reduced epithelial delamination. Additionally, we hypothesized a role for ENaC-mediated Na^+ reabsorption as a mechanism participating in dome formation. ENaC has been studied in dome formation of other kidney and non-kidney cell lines. In MDCK cells, NHE3 and ENaCα protein expression was increased from *day 1* to *day 5* following growth to cell confluence (84), ENaCβ protein expression was required for dome formation in rat mammary cells (106), and 10 nM to 10 μM amiloride and 10 nM BZ reduced dome formation in cultured keratinocytes (6). In our 3D CCD, BZ decreased dome number and size. The inhibitory effects of BZ and a drainage channel on cell doming suggests multiple mechanisms for this phenomenon in the 3D CCD, which involves both Na^+ transport and epithelial delamination.

In isolated in vitro microperfused CCDs, ENaC-mediated Na^+ reabsorption is stimulated by high tubular flow rates (55, 79). Hence, perfusion of the 3D CCD at high luminal flow rates would be expected to stimulate Na^+ absorption into the ECM. Water reabsorption in the native mammalian CD is dependent on the high interstitial osmolality, established in part by Na^+ reabsorption, in the setting of apical AQP2 on PCs (59, 75, 82). We speculate that ENaC-mediated Na^+ reabsorption can lead to fluid reabsorption into the ECM, as has been demonstrated in cultured $mCCD_{cl1}$ cells grown on Transwells (24). When luminal flow ceases in 3D CCDs without drainage channels, the resulting luminal hydrostatic pressure drop is expected to give rise to a back pressure exerted by the "absorbed" volume in the ECM, which induces epithelial delamination and doming into the lumen. By contrast, in the presence of a drainage channel, this back pressure is quickly dissipated thereby mitigating delamination and doming phenomena. Our observations that BZ decreases dome number and size are consistent with a role of ENaC in facilitating volume absorption into the ECM. Future studies that compare cell doming under low and high flow rates may provide new insights regarding the flow regulation of ENaC in our 3D CCD model.

Transepithelial Na^+ transport in isolated in vitro microperfused tubules can be quantified indirectly by measuring transepithelial voltage or directly by measuring Na^+ concentrations in samples (nanoliters) of collected tubular fluid by helium glow photometry, ion chromatography, microfluorimetry, or electrophysiologically with ion-selective microelectrodes. To date, the quantification of solute transport in microphysiological models has largely focused on proximal tubules, but analyses of Na^+ transport are limited. Using a multilayer microfluidic device with primary cultures of rat IMCD cells, the osmolarity of apical effluent increased upon exposure to basolateral vasopressin and the apical Na^+ concentration decreased upon exposure to basolateral aldosterone, suggestive of water and Na^+ reabsorption (34). Apical effluent was collected over 1 h and osmolarity and Na^+ concentration were determined using an osmometer and an inductively coupled plasma emission spectrometer, respectively. In proximal tubule and thick ascending limb models, no detectable difference was observed in reservoir Na^+ and Cl^- concentrations after 4 days of continuous perfusion. Transport was detected using integrated electrodes to perform electrical impedance spectroscopy upon exposure to a transepithelial NaCl gradient (105). Specific channel or transporter inhibitors were not used to further characterize the transport pathways involved.

Among proximal tubule models, methods to quantify glucose reabsorption have included *1*) direct measurement of serial media reservoir samples (50) or microfluidic effluent (17, 33), *2*) the use of the fluorescent glucose analog 2-NBDG to detect changes in intracellular (90, 93) or basolateral (69, 88) fluorescence intensities over time, and *3*) the use of 2-deoxyglucose to determine glucose uptake with a colorimetric assay (37) either in the presence or absence of Na^+ glucose cotransporter 2 (SGLT2) inhibitors or ouabain, an inhibitor of Na^+/K^+-ATPase. Besides glucose transport, secretory and reabsorptive functional assays have been reported in which the ammonia (73, 93), albumin (30, 33, 35, 50, 69), para-aminohippurate (93), and indoxyl sulfate (35, 93) are analyzed using fluophores, colorimetric assays, or radioactive tracers.

In its current configuration, our 3D CCD model does not allow for sequential and reproducible measurements of transepithelial voltage. When metal electrodes were placed within the ECM to carry out such measurements, we found that that the electrical current was short circuited. Efforts are now underway to develop a new technique for quantifying transepithelial ion transport as well as the flow-dependent effects of ENaC-mediated Na^+ reabsorption and K^+ secretion using in situ microelectrodes, functional fluorescent reporter dyes, and direct measurement of ion concentrations in the microfluidic effluent and reservoir media.

Looking ahead, our 3D CCD model is well suited for studying physiologically relevant hydrodynamic forces that may regulate cell function in vivo, akin to in vitro microperfused mammalian tubules. As the native CD is a unique nephron segment with a heterogeneous cell population, our 3D CCDs provide a unique microphysiological model for studying cell-specific contributions to transport and autocrine/paracrine signaling. However, comparisons between our 3D CCDs and isolated in vitro microperfused tubules should be made with caution. Our current 3D CCD is solely composed of PC-like mpkCCD cells and lacks ICs, which in the native epithelium regulate PC function via autocrine/paracrine signaling by factors such as ATP and prostaglandin E_2 (40). We do not yet know which, if any, autocrine/paracrine signaling factors are generated in the 3D CCD. Additionally, our model may serve as a novel platform to develop cell culture models of hydronephrosis, cystic kidney diseases, and other pathologies associated with circumferential tubule dilation, where existing models are largely limited to convex stretch applied to 2D epithelial monolayers or 3D cell cultures without fluid flow (15, 18).

In summary, our 3D CCD model offers a geometrically appropriate cell-culture model to study, under physiologically relevant conditions, cellular function characteristic of the native mammalian CCD, a segment whose functions in fluid, electrolyte, and acid/base homeostasis (9) and inflammation (5) continue to be discovered. 3D CCDs composed of unique cell types should allow us to define contributions of specific cell populations and discrete hydrodynamic forces, prevalent in the native epithelium, to cell-specific function in the ASDN.

ACKNOWLEDGMENTS

Light and fluorescent microscopy and 3D image rendering were performed at the Microscopy CoRE and histology was performed at the Biorepository and Pathology CoRE at the Icahn School of Medicine at Mount Sinai (ISMMS). Transmission electron microscopy was performed at the Harvard Medical School EM Facility. We acknowledge *1*) from Harvard University: David Kolesky, Katharina Kroll, and Sanlin Robinson for assistance and advice and Lori K. Sanders for photography and videography; *2*) from ISMMS: Nikos Tzavaras, Esperanza Agullo Pascual, and Nasim Jamali for microscopy expertise and Jill K. Gregory for illustrations; and *3*) Alain Vandewalle from INSERM for the mpkCCD cell line.

GRANTS

This work was supported in part by NIH National Institute of Diabetes and Digestive and Kidney Diseases (NIDDK) Grant T32DK007757 (J.L.R.), NIDDK (Re)Building A Kidney Consortium Grants U01DK107350 (L.M.S.) and R56DK122380 (J.A.L.), NIDDK Grants R01DK038470 (L.M.S.) and P30DK079307 (L.M.S.) (The Pittsburgh Center for Kidney Research; PI, Tom Kleyman), and NIH National Center for Advancing Translational Sciences Grant UG3TR002155 (N.Y.C.L. and J.A.L.).

DISCLOSURES

J. A. Lewis has cofounded two companies, Electroninks, Inc. and Voxel8, Inc., which focused on printing advanced materials. None of the other authors has any conflicts of interest, financial or otherwise, to disclose.

AUTHOR CONTRIBUTIONS

J.L.R., D.F., R.C.-G., N.Y.C.L., K.A.H., J.A.L., and L.M.S. conceived and designed research; J.L.R., S.H., D.F., and N.Y.C.L. performed experiments; J.L.R., R.C.-G., and L.M.S. analyzed data; J.L.R., D.F., R.C.-G., N.Y.C.L., K.A.H., J.A.L., and L.M.S. interpreted results of experiments; J.L.R., R.C.-G., N.Y.C.L., J.A.L., and L.M.S. prepared figures; J.L.R. and L.M.S. drafted manuscript; J.L.R., N.Y.C.L., K.A.H., J.A.L., and L.M.S. edited and revised manuscript; J.L.R., S.H., D.F., R.C.-G., N.Y.C.L., K.A.H., J.A.L., and L.M.S. approved final version of manuscript.

REFERENCES

1. **Adler M, Ramm S, Hafner M, Muhlich JL, Gottwald EM, Weber E, Jaklic A, Ajay AK, Svoboda D, Auerbach S, Kelly EJ, Himmelfarb J, Vaidya VS.** A quantitative approach to screen for nephrotoxic compounds in vitro. *J Am Soc Nephrol* 27: 1015–1028, 2016. doi:10.1681/ASN.2015010060.
2. **Alli AA, Bao HF, Liu BC, Yu L, Aldrugh S, Montgomery DS, Ma HP, Eaton DC.** Calmodulin and CaMKII modulate ENaC activity by regulating the association of MARCKS and the cytoskeleton with the apical membrane. *Am J Physiol Renal Physiol* 309: F456–F463, 2015. doi:10.1152/ajprenal.00631.2014.
3. **Assmus AM, Mansley MK, Mullins LJ, Peter A, Mullins JJ.** mCCD$_{cl1}$ cells show plasticity consistent with the ability to transition between principal and intercalated cells. *Am J Physiol Renal Physiol* 314: F820–F831, 2018. doi:10.1152/ajprenal.00354.2017.
4. **Bens M, Vallet V, Cluzeaud F, Pascual-Letallec L, Kahn A, Rafestin-Oblin ME, Rossier BC, Vandewalle A.** Corticosteroid-dependent sodium transport in a novel immortalized mouse collecting duct principal cell line. *J Am Soc Nephrol* 10: 923–934, 1999.
5. **Breton S, Brown D.** Novel proinflammatory function of renal intercalated cells. *Ann Nutr Metab* 72, *Suppl* 2: 11–16, 2018. doi:10.1159/000488303.
6. **Brouard M, Casado M, Djelidi S, Barrandon Y, Farman N.** Epithelial sodium channel in human epidermal keratinocytes: expression of its subunits and relation to sodium transport and differentiation. *J Cell Sci* 112: 3343–3352, 1999.
7. **Burg M, Grantham J, Abramow M, Orloff J.** Preparation and study of fragments of single rabbit nephrons. *Am J Physiol* 210: 1293–1298, 1966. doi:10.1152/ajplegacy.1966.210.6.1293.
8. **Burg MB, Knepper MA.** Single tubule perfusion techniques. *Kidney Int* 30: 166–170, 1986. doi:10.1038/ki.1986.168.
9. **Carrisoza-Gaytan R, Carattino MD, Kleyman TR, Satlin LM.** An unexpected journey: conceptual evolution of mechanoregulated potassium transport in the distal nephron. *Am J Physiol Cell Physiol* 310: C243–C259, 2016. doi:10.1152/ajpcell.00328.2015.
10. **Carrisoza-Gaytan R, Liu Y, Flores D, Else C, Lee HG, Rhodes G, Sandoval RM, Kleyman TR, Lee FY, Molitoris B, Satlin LM, Rohatgi R.** Effects of biomechanical forces on signaling in the cortical collecting duct (CCD). *Am J Physiol Renal Physiol* 307: F195–F204, 2014. doi:10.1152/ajprenal.00634.2013.
11. **Carrisoza-Gaytan R, Ray EC, Flores D, Marciszyn AL, Wu P, Liu L, Subramanya AR, Wang W, Sheng S, Nkashama LJ, Chen J, Jackson EK, Mutchler SM, Heja S, Kohan DE, Satlin LM, Kleyman TR.** Intercalated cell BKα subunit is required for flow-induced K+ secretion. *JCI Insight* 5: e130553, 2020. doi:10.1172/jci.insight.130553.
12. **Carrisoza-Gaytán R, Wang L, Schreck C, Kleyman TR, Wang WH, Satlin LM.** The mechanosensitive BKα/β1 channel localizes to cilia of principal cells in rabbit cortical collecting duct (CCD). *Am J Physiol Renal Physiol* 312: F143–F156, 2017. doi:10.1152/ajprenal.00256.2016.
13. **Cattaneo I, Condorelli L, Terrinoni AR, Antiga L, Sangalli F, Remuzzi A.** Shear stress reverses dome formation in confluent renal tubular cells. *Cell Physiol Biochem* 28: 673–682, 2011. doi:10.1159/000335813.
14. **Chen L, Lee JW, Chou CL, Nair AV, Battistone MA, Păunescu TG, Merkulova M, Breton S, Verlander JW, Wall SM, Brown D, Burg MB, Knepper MA.** Transcriptomes of major renal collecting duct cell types in mouse identified by single-cell RNA-seq. *Proc Natl Acad Sci USA* 114: E9989–E9998, 2017. doi:10.1073/pnas.1710964114.
15. **Chevalier RL.** Obstructive nephropathy: towards biomarker discovery and gene therapy. *Nat Clin Pract Nephrol* 2: 157–168, 2006. doi:10.1038/ncpneph0098.
16. **Chrobak KM, Potter DR, Tien J.** Formation of perfused, functional microvascular tubes in vitro. *Microvasc Res* 71: 185–196, 2006. doi:10.1016/j.mvr.2006.02.005.
17. **Curto VF, Marchiori B, Hama A, Pappa AM, Ferro MP, Braendlein M, Rivnay J, Fiocchi M, Malliaras GG, Ramuz M, Owens RM.** Organic transistor platform with integrated microfluidics for in-line multi-parametric *in vitro* cell monitoring. *Microsyst Nanoeng* 3: 17028, 2017. doi:10.1038/micronano.2017.28.
18. **Dixon EE, Woodward OM.** Three-dimensional in vitro models answer the right questions in ADPKD cystogenesis. *Am J Physiol Renal Physiol* 315: F332–F335, 2018. doi:10.1152/ajprenal.00126.2018.
19. **Dreher D, Rochat T.** Hyperoxia induces alkalinization and dome formation in MDCK epithelial cells. *Am J Physiol Cell Physiol* 262: C358–C364, 1992. doi:10.1152/ajpcell.1992.262.2.C358.
20. **Duan Y, Gotoh N, Yan Q, Du Z, Weinstein AM, Wang T, Weinbaum S.** Shear-induced reorganization of renal proximal tubule cell actin cytoskeleton and apical junctional complexes. *Proc Natl Acad Sci USA* 105: 11418–11423, 2008. doi:10.1073/pnas.0804954105.
21. **Duan Y, Weinstein AM, Weinbaum S, Wang T.** Shear stress-induced changes of membrane transporter localization and expression in mouse proximal tubule cells. *Proc Natl Acad Sci USA* 107: 21860–21865, 2010. doi:10.1073/pnas.1015751107.
22. **Fejes-Tóth G, Náray-Fejes-Tóth A.** Differentiation of renal beta-intercalated cells to alpha-intercalated and principal cells in culture. *Proc Natl Acad Sci USA* 89: 5487–5491, 1992. doi:10.1073/pnas.89.12.5487.
23. **Flores D, Liu Y, Liu W, Satlin LM, Rohatgi R.** Flow-induced prostaglandin E2 release regulates Na and K transport in the collecting duct. *Am J Physiol Renal Physiol* 303: F632–F638, 2012. doi:10.1152/ajprenal.00169.2012.
24. **Gaeggeler HP, Guillod Y, Loffing-Cueni D, Loffing J, Rossier BC.** Vasopressin-dependent coupling between sodium transport and water flow in a mouse cortical collecting duct cell line. *Kidney Int* 79: 843–852, 2011. doi:10.1038/ki.2010.486.
25. **Grantham JJ, Burg MB.** Effect of vasopressin and cyclic AMP on permeability of isolated collecting tubules. *Am J Physiol* 211: 255–259, 1966. doi:10.1152/ajplegacy.1966.211.1.255.
26. **Grantham JJ, Geiser JL, Evan AP.** Cyst formation and growth in autosomal dominant polycystic kidney disease. *Kidney Int* 31: 1145–1152, 1987. doi:10.1038/ki.1987.121.
27. **Gross JB, Imai M, Kokko JP.** A functional comparison of the cortical collecting tubule and the distal convoluted tubule. *J Clin Invest* 55: 1284–1294, 1975. doi:10.1172/JCI108048.

28. **Hebert SC, Andreoli TE.** Water movement across the mammalian cortical collecting duct. *Kidney Int* 22: 526–535, 1982. doi:10.1038/ki.1982.206.
29. **Homan KA, Gupta N, Kroll KT, Kolesky DB, Skylar-Scott M, Miyoshi T, Mau D, Valerius MT, Ferrante T, Bonventre JV, Lewis JA, Morizane R.** Flow-enhanced vascularization and maturation of kidney organoids in vitro. *Nat Methods* 16: 255–262, 2019. doi:10.1038/s41592-019-0325-y.
30. **Homan KA, Kolesky DB, Skylar-Scott MA, Herrmann J, Obuobi H, Moisan A, Lewis JA.** Bioprinting of 3D Convoluted Renal Proximal Tubules on Perfusable Chips. *Sci Rep* 6: 34845, 2016. doi:10.1038/srep34845.
31. **Ilatovskaya DV, Pavlov TS, Levchenko V, Negulyaev YA, Staruschenko A.** Cortical actin binding protein cortactin mediates ENaC activity via Arp2/3 complex. *FASEB J* 25: 2688–2699, 2011. doi:10.1096/fj.10-167262.
32. **Jang KJ, Cho HS, Kang DH, Bae WG, Kwon TH, Suh KY.** Fluid-shear-stress-induced translocation of aquaporin-2 and reorganization of actin cytoskeleton in renal tubular epithelial cells. *Integr Biol* 3: 134–141, 2011. doi:10.1039/C0IB00018C.
33. **Jang KJ, Mehr AP, Hamilton GA, McPartlin LA, Chung S, Suh KY, Ingber DE.** Human kidney proximal tubule-on-a-chip for drug transport and nephrotoxicity assessment. *Integr Biol* 5: 1119–1129, 2013. doi:10.1039/c3ib40049b.
34. **Jang KJ, Suh KY.** A multi-layer microfluidic device for efficient culture and analysis of renal tubular cells. *Lab Chip* 10: 36–42, 2010. doi:10.1039/B907515A.
35. **Jansen J, Fedecostante M, Wilmer MJ, Peters JG, Kreuser UM, van den Broek PH, Mensink RA, Boltje TJ, Stamatialis D, Wetzels JF, van den Heuvel LP, Hoenderop JG, Masereeuw R.** Bioengineered kidney tubules efficiently excrete uremic toxins. *Sci Rep* 6: 26715, 2016. doi:10.1038/srep26715.
36. **Jung HJ, Kwon TH.** Molecular mechanisms regulating aquaporin-2 in kidney collecting duct. *Am J Physiol Renal Physiol* 311: F1318–F1328, 2016. doi:10.1152/ajprenal.00485.2016.
37. **King SM, Higgins JW, Nino CR, Smith TR, Paffenroth EH, Fairbairn CE, Docuyanan A, Shah VD, Chen AE, Presnell SC, Nguyen DG.** 3D proximal tubule tissues recapitulate key aspects of renal physiology to enable nephrotoxicity testing. *Front Physiol* 8: 123, 2017. doi:10.3389/fphys.2017.00123.
38. **Kinoshita Y, Fukase M, Miyauchi A, Nakada M, Takenaka M, Fujita T.** Effect of aldosterone on dome formation by MDCK mono-layer. *Endocrinol Jpn* 33: 317–322, 1986. doi:10.1507/endocrj1954.33.317.
39. **Kleyman TR, Cragoe EJ Jr.** Amiloride and its analogs as tools in the study of ion transport. *J Membr Biol* 105: 1–21, 1988. doi:10.1007/BF01871102.
40. **Kleyman TR, Satlin LM, Hallows KR.** Opening lines of communication in the distal nephron. *J Clin Invest* 123: 4139–4141, 2013. doi:10.1172/JCI71944.
41. **Knepper MA, Kwon TH, Nielsen S.** Molecular physiology of water balance. *N Engl J Med* 372: 1349–1358, 2015. doi:10.1056/NEJMra1404726.
42. **Kolesky DB, Homan KA, Skylar-Scott MA, Lewis JA.** Three-dimensional bioprinting of thick vascularized tissues. *Proc Natl Acad Sci USA* 113: 3179–3184, 2016. doi:10.1073/pnas.1521342113.
43. **Kriz W, Bankir L; The Renal Commission of the International Union of Physiological Sciences (IUPS).** A standard nomenclature for structures of the kidney. *Kidney Int* 33: 1–7, 1988. doi:10.1038/ki.1988.1.
44. **Latorre E, Kale S, Casares L, Gómez-González M, Uroz M, Valon L, Nair RV, Garreta E, Montserrat N, Del Campo A, Ladoux B, Arroyo M, Trepat X.** Active superelasticity in three-dimensional epithelia of controlled shape. *Nature* 563: 203–208, 2018. doi:10.1038/s41586-018-0671-4.
45. **Layton AT, Layton HE.** A computational model of epithelial solute and water transport along a human nephron. *PLOS Comput Biol* 15: e1006108, 2019. doi:10.1371/journal.pcbi.1006108.
46. **Leighton J, Brada Z, Estes LW, Justh G.** Secretory activity and oncogenicity of a cell line (MDCK) derived from canine kidney. *Science* 163: 472–473, 1969. doi:10.1126/science.163.3866.472.
47. **Lever JE.** Inducers of mammalian cell differentiation stimulate dome formation in a differentiated kidney epithelial cell line (MDCK). *Proc Natl Acad Sci USA* 76: 1323–1327, 1979. doi:10.1073/pnas.76.3.1323.
48. **Lifschitz MD.** Prostaglandins may mediate chloride concentration gradient across domes formed by MDCK1 cells. *Am J Physiol Renal Physiol* 250: F525–F531, 1986. doi:10.1152/ajprenal.1986.250.3.F525.
49. **Ligresti G, Nagao RJ, Xue J, Choi YJ, Xu J, Ren S, Aburatani T, Anderson SK, MacDonald JW, Bammler TK, Schwartz SM, Muczynski KA, Duffield JS, Himmelfarb J, Zheng Y.** A novel three-dimensional human peritubular microvascular system. *J Am Soc Nephrol* 27: 2370–2381, 2016. doi:10.1681/ASN.2015070747.
50. **Lin NY, Homan KA, Robinson SS, Kolesky DB, Duarte N, Moisan A, Lewis JA.** Renal reabsorption in 3D vascularized proximal tubule models. *Proc Natl Acad Sci USA* 116: 5399–5404, 2019. doi:10.1073/pnas.1815208116.
51. **Liu W, Xu S, Woda C, Kim P, Weinbaum S, Satlin LM.** Effect of flow and stretch on the [Ca2+]i response of principal and intercalated cells in cortical collecting duct. *Am J Physiol Renal Physiol* 285: F998–F1012, 2003. doi:10.1152/ajprenal.00067.2003.
52. **Maechler FA, Allier C, Roux A, Tomba C.** Curvature-dependent constraints drive remodeling of epithelia. *J Cell Sci* 132: jcs222372, 2019. doi:10.1242/jcs.222372.
53. **Mazzochi C, Bubien JK, Smith PR, Benos DJ.** The carboxyl terminus of the alpha-subunit of the amiloride-sensitive epithelial sodium channel binds to F-actin. *J Biol Chem* 281: 6528–6538, 2006. doi:10.1074/jbc.M509386200.
54. **Miner JH.** Renal basement membrane components. *Kidney Int* 56: 2016–2024, 1999. doi:10.1046/j.1523-1755.1999.00785.x.
55. **Morimoto T, Liu W, Woda C, Carattino MD, Wei Y, Hughey RP, Apodaca G, Satlin LM, Kleyman TR.** Mechanism underlying flow stimulation of sodium absorption in the mammalian collecting duct. *Am J Physiol Renal Physiol* 291: F663–F669, 2006. doi:10.1152/ajprenal.00514.2005.
56. **Morla L, Doucet A, Lamouroux C, Crambert G, Edwards A.** The renal cortical collecting duct: a secreting epithelium? *J Physiol* 594: 5991–6008, 2016. doi:10.1113/JP272877.
57. **Mukherjee M, deRiso J, Otterpohl K, Ratnayake I, Kota D, Ahrenkiel P, Chandrasekar I, Surendran K.** Endogenous notch signaling in adult kidneys maintains segment-specific epithelial cell types of the distal tubules and collecting ducts to ensure water homeostasis. *J Am Soc Nephrol* 30: 110–126, 2019. doi:10.1681/ASN.2018040440.
58. **Myers CE, Bulger RE, Tisher CC, Trump BF.** Human ultrastructure. IV. Collecting duct of healthy individuals. *Lab Invest* 15: 1921–1950, 1966.
59. **Nielsen S, Frøkiaer J, Marples D, Kwon TH, Agre P, Knepper MA.** Aquaporins in the kidney: from molecules to medicine. *Physiol Rev* 82: 205–244, 2002. doi:10.1152/physrev.00024.2001.
60. **Nouwen EJ, De Broe ME.** EGF and TGF-alpha in the human kidney: identification of octopal cells in the collecting duct. *Kidney Int* 45: 1510–1521, 1994. doi:10.1038/ki.1994.198.
61. **Oberleithner H, Vogel U, Kersting U.** Madin-Darby canine kidney cells. I. Aldosterone-induced domes and their evaluation as a model system. *Pflügers Arch* 416: 526–532, 1990. doi:10.1007/BF00382685.
62. **Oberleithner H, Vogel U, Kersting U, Steigner W.** Madin-Darby canine kidney cells. II. Aldosterone stimulates Na^+/H^+ and Cl^-/HCO_3^--exchange. *Pflügers Arch* 416: 533–539, 1990. doi:10.1007/BF00382686.
63. **Palmer LG, Schnermann J.** Integrated control of Na transport along the nephron. *Clin J Am Soc Nephrol* 10: 676–687, 2015. doi:10.2215/CJN.12391213.
64. **Park J, Shrestha R, Qiu C, Kondo A, Huang S, Werth M, Li M, Barasch J, Suszták K.** Single-cell transcriptomics of the mouse kidney reveals potential cellular targets of kidney disease. *Science* 360: 758–763, 2018. doi:10.1126/science.aar2131.
65. **Pearce D, Soundararajan R, Trimpert C, Kashlan OB, Deen PM, Kohan DE.** Collecting duct principal cell transport processes and their regulation. *Clin J Am Soc Nephrol* 10: 135–146, 2015. doi:10.2215/CJN.05760513.
66. **Price GM, Tien J.** Methods for forming human microvascular tubes in vitro and measuring their macromolecular permeability. *Methods Mol Biol* 671: 281–293, 2011. doi:10.1007/978-1-59745-551-0_17.
67. **Raghavan V, Rbaibi Y, Pastor-Soler NM, Carattino MD, Weisz OA.** Shear stress-dependent regulation of apical endocytosis in renal proximal tubule cells mediated by primary cilia. *Proc Natl Acad Sci USA* 111: 8506–8511, 2014. [Erratum in *Proc Natl Acad Sci USA* 113: E1587, 2016.] doi:10.1073/pnas.1402195111.

68. **Rao R, Bhalla V, Pastor-Soler NM.** Intercalated cells of the kidney collecting duct in kidney physiology. *Semin Nephrol* 39: 353–367, 2019. doi:10.1016/j.semnephrol.2019.04.005.
69. **Rayner SG, Phong KT, Xue J, Lih D, Shankland SJ, Kelly EJ, Himmelfarb J, Zheng Y.** Reconstructing the human renal vascular-tubular unit in vitro. *Adv Healthc Mater* 7: 1801120, 2018. doi:10.1002/adhm.201801120.
70. **Rinschen MM, Yu MJ, Wang G, Boja ES, Hoffert JD, Pisitkun T, Knepper MA.** Quantitative phosphoproteomic analysis reveals vasopressin V2-receptor-dependent signaling pathways in renal collecting duct cells. *Proc Natl Acad Sci USA* 107: 3882–3887, 2010. doi:10.1073/pnas.0910646107.
71. **Robert-Nicoud M, Flahaut M, Elalouf JM, Nicod M, Salinas M, Bens M, Doucet A, Wincker P, Artiguenave F, Horisberger JD, Vandewalle A, Rossier BC, Firsov D.** Transcriptome of a mouse kidney cortical collecting duct cell line: effects of aldosterone and vasopressin. *Proc Natl Acad Sci USA* 98: 2712–2716, 2001. doi:10.1073/pnas.051603198.
72. **Roy A, Al-bataineh MM, Pastor-Soler NM.** Collecting duct intercalated cell function and regulation. *Clin J Am Soc Nephrol* 10: 305–324, 2015. doi:10.2215/CJN.08880914.
73. **Sakolish C, Weber EJ, Kelly EJ, Himmelfarb J, Mouneimne R, Grimm FA, House JS, Wade T, Han A, Chiu WA, Rusyn I.** Technology transfer of the microphysiological systems: a case study of the human proximal tubule tissue chip. *Sci Rep* 8: 14882, 2018. doi:10.1038/s41598-018-33099-2.
74. **Sandoval PC, Slentz DH, Pisitkun T, Saeed F, Hoffert JD, Knepper MA.** Proteome-wide measurement of protein half-lives and translation rates in vasopressin-sensitive collecting duct cells. *J Am Soc Nephrol* 24: 1793–1805, 2013. doi:10.1681/ASN.2013030279.
75. **Sands JM, Layton HE.** Advances in understanding the urine-concentrating mechanism. *Annu Rev Physiol* 76: 387–409, 2014. doi:10.1146/annurev-physiol-021113-170350.
76. **Satlin LM, Carattino MD, Liu W, Kleyman TR.** Regulation of cation transport in the distal nephron by mechanical forces. *Am J Physiol Renal Physiol* 291: F923–F931, 2006. doi:10.1152/ajprenal.00192.2006.
77. **Satlin LM, Evan AP, Gattone VH 3rd, Schwartz GJ.** Postnatal maturation of the rabbit cortical collecting duct. *Pediatr Nephrol* 2: 135–145, 1988. doi:10.1007/BF00870394.
78. **Satlin LM, Schwartz GJ.** Postnatal maturation of rabbit renal collecting duct: intercalated cell function. *Am J Physiol Renal Physiol* 253: F622–F635, 1987. doi:10.1152/ajprenal.1987.253.4.F622.
79. **Satlin LM, Sheng S, Woda CB, Kleyman TR.** Epithelial Na^+ channels are regulated by flow. *Am J Physiol Renal Physiol* 280: F1010–F1018, 2001. doi:10.1152/ajprenal.2001.280.6.F1010.
80. **Schenk LK, Bolger SJ, Luginbuhl K, Gonzales PA, Rinschen MM, Yu MJ, Hoffert JD, Pisitkun T, Knepper MA.** Quantitative proteomics identifies vasopressin-responsive nuclear proteins in collecting duct cells. *J Am Soc Nephrol* 23: 1008–1018, 2012. doi:10.1681/ASN.2011070738.
81. **Simon H, Gao Y, Franki N, Hays RM.** Vasopressin depolymerizes apical F-actin in rat inner medullary collecting duct. *Am J Physiol Cell Physiol* 265: C757–C762, 1993. doi:10.1152/ajpcell.1993.265.3.C757.
82. **Spring KR.** Routes and mechanism of fluid transport by epithelia. *Annu Rev Physiol* 60: 105–119, 1998. doi:10.1146/annurev.physiol.60.1.105.
83. **Su HW, Wang SW, Ghishan FK, Kiela PR, Tang MJ.** Cell confluency-induced Stat3 activation regulates NHE3 expression by recruiting Sp1 and Sp3 to the proximal NHE3 promoter region during epithelial dome formation. *Am J Physiol Cell Physiol* 296: C13–C24, 2009. doi:10.1152/ajpcell.00263.2008.
84. **Su HW, Yeh HH, Wang SW, Shen MR, Chen TL, Kiela PR, Ghishan FK, Tang MJ.** Cell confluence-induced activation of signal transducer and activator of transcription-3 (Stat3) triggers epithelial dome formation via augmentation of sodium hydrogen exchanger-3 (NHE3) expression. *J Biol Chem* 282: 9883–9894, 2007. doi:10.1074/jbc.M606754200.
85. **Sugahara K, Caldwell JH, Mason RJ.** Electrical currents flow out of domes formed by cultured epithelial cells. *J Cell Biol* 99: 1541–1544, 1984. doi:10.1083/jcb.99.4.1541.
86. **Théry M, Asnacios A.** Cellular stretch reveals superelastic powers. *Nature* 563: 192–194, 2018. doi:10.1038/d41586-018-07172-9.
87. **Tian L, Chen L, McClafferty H, Sailer CA, Ruth P, Knaus HG, Shipston MJ, Tian L, Chen L, McClafferty H, Sailer CA, Ruth P, Knaus HG, Shipston MJ.** A noncanonical SH3 domain binding motif links BK channels to the actin cytoskeleton via the SH3 adapter cortactin. *FASEB J* 20: 2588–2590, 2006. doi:10.1096/fj.06-6152fje.
88. **Vedula EM, Alonso JL, Arnaout MA, Charest JL.** A microfluidic renal proximal tubule with active reabsorptive function. *PLoS One* 12: e0184330, 2017. doi:10.1371/journal.pone.0184330.
89. **Venzac B, Madoun R, Benarab T, Monnier S, Cayrac F, Myram S, Leconte L, Amblard F, Viovy JL, Descroix S, Coscoy S.** Engineering small tubes with changes in diameter for the study of kidney cell organization. *Biomicrofluidics* 12: 024114, 2018. doi:10.1063/1.5025027.
90. **Vormann MK, Gijzen L, Hutter S, Boot L, Nicolas A, van den Heuvel A, Vriend J, Ng CP, Nieskens TT, van Duinen V, de Wagenaar B, Masereeuw R, Suter-Dick L, Trietsch SJ, Wilmer M, Joore J, Vulto P, Lanz HL.** Nephrotoxicity and kidney transport assessment on 3D perfused proximal tubules. *AAPS J* 20: 90, 2018. doi:10.1208/s12248-018-0248-z.
91. **Wall SM.** The role of pendrin in blood pressure regulation. *Am J Physiol Renal Physiol* 310: F193–F203, 2016. doi:10.1152/ajprenal.00400.2015.
92. **Wang WH, Cassola A, Giebisch G.** Involvement of actin cytoskeleton in modulation of apical K channel activity in rat collecting duct. *Am J Physiol Renal Physiol* 267: F592–F598, 1994. doi:10.1152/ajprenal.1994.267.4.F592.
93. **Weber EJ, Chapron A, Chapron BD, Voellinger JL, Lidberg KA, Yeung CK, Wang Z, Yamaura Y, Hailey DW, Neumann T, Shen DD, Thummel KE, Muczynski KA, Himmelfarb J, Kelly EJ.** Development of a microphysiological model of human kidney proximal tubule function. *Kidney Int* 90: 627–637, 2016. doi:10.1016/j.kint.2016.06.011.
94. **Weinbaum S, Duan Y, Satlin LM, Wang T, Weinstein AM.** Mechanotransduction in the renal tubule. *Am J Physiol Renal Physiol* 299: F1220–F1236, 2010. doi:10.1152/ajprenal.00453.2010.
95. **Welling LW, Evan AP, Welling DJ.** Shape of cells and extracellular channels in rabbit cortical collecting ducts. *Kidney Int* 20: 211–222, 1981. doi:10.1038/ki.1981.123.
96. **Welling LW, Evan AP, Welling DJ, Gattone VH 3rd.** Morphometric comparison of rabbit cortical connecting tubules and collecting ducts. *Kidney Int* 23: 358–367, 1983. doi:10.1038/ki.1983.27.
97. **Welling LW, Grantham JJ.** Physical properties of isolated perfused renal tubules and tubular basement membranes. *J Clin Invest* 51: 1063–1075, 1972. doi:10.1172/JCI106898.
98. **Whiting JL, Ogier L, Forbush KA, Bucko P, Gopalan J, Seternes OM, Langeberg LK, Scott JD.** AKAP220 manages apical actin networks that coordinate aquaporin-2 location and renal water reabsorption. *Proc Natl Acad Sci USA* 113: E4328–E4337, 2016. doi:10.1073/pnas.1607745113.
99. **Woda CB, Bragin A, Kleyman TR, Satlin LM.** Flow-dependent K^+ secretion in the cortical collecting duct is mediated by a maxi-K channel. *Am J Physiol Renal Physiol* 280: F786–F793, 2001. doi:10.1152/ajprenal.2001.280.5.F786.
100. **Woda CB, Leite M Jr, Rohatgi R, Satlin LM.** Effects of luminal flow and nucleotides on [Ca(2+)](i) in rabbit cortical collecting duct. *Am J Physiol Renal Physiol* 283: F437–F446, 2002. doi:10.1152/ajprenal.00316.2001.
101. **Woda CB, Miyawaki N, Ramalakshmi S, Ramkumar M, Rojas R, Zavilowitz B, Kleyman TR, Satlin LM.** Ontogeny of flow-stimulated potassium secretion in rabbit cortical collecting duct: functional and molecular aspects. *Am J Physiol Renal Physiol* 285: F629–F639, 2003. doi:10.1152/ajprenal.00191.2003.
102. **Wong KH, Truslow JG, Khankhel AH, Chan KL, Tien J.** Artificial lymphatic drainage systems for vascularized microfluidic scaffolds. *J Biomed Mater Res A* 101A: 2181–2190, 2013. doi:10.1002/jbm.a.34524.
103. **Xi W, Sonam S, Beng Saw T, Ladoux B, Teck Lim C.** Emergent patterns of collective cell migration under tubular confinement. *Nat Commun* 8: 1517, 2017. doi:10.1038/s41467-017-01390-x.
104. **Yanagawa N, Trizna W, Bar-Khayim Y, Fine LG.** Effects of vasopressin on the isolated perfused human collecting tubule. *Kidney Int* 19: 705–709, 1981. doi:10.1038/ki.1981.70.
105. **Yeste J, Martínez-Gimeno L, Illa X, Laborda P, Guimerà A, Sánchez-Marín JP, Villa R, Giménez I.** A perfusion chamber for monitoring transepithelial NaCl transport in an in vitro model of the renal tubule. *Biotechnol Bioeng* 115: 1604–1613, 2018. doi:10.1002/bit.26574.
106. **Zucchi I, Bini L, Valaperta R, Ginestra A, Albani D, Susani L, Sanchez JC, Liberatori S, Magi B, Raggiaschi R, Hochstrasser DF, Pallini V, Vezzoni P, Dulbecco R.** Proteomic dissection of dome formation in a mammary cell line: role of tropomyosin-5b and maspin. *Proc Natl Acad Sci USA* 98: 5608–5613, 2001. doi:10.1073/pnas.091101898.